Observer-based controller for floor vibration control with optimisation algorithms

Donald S Nyawako[1] and Paul Reynolds[1, 2]

Abstract

This study presents the results of vibration suppression of a walkway bridge structure with a single actuator and sensor pair by using a proportional-integral (PI) controller and observer-based pole-placement controllers. From the results of experimental modal analysis (EMA), reduced order models of the walkway are identified. These are used for the design of a PI controller as well as for state estimation procedures that are necessary for development of reduced-order observer controllers. The respective orders of the latter are dependent on the number of plant modes used for their designs. They are formulated from plant and observer feedback gains that are obtained from specification of desired floor closed-loop eigenvalues and observer eigenvalues. There are numerous solutions possible with the observer-based controller design procedures whereas the PI controller defaults to a particular solution. There is also the flexibility for isolation and control of target vibration modes with the observer-based controllers for higher controller orders from a purely single-input single-output controller scheme as demonstrated in the analytical and experimental studies presented. Further, in this work, a design space of potential feedback gains is specified, where only a single plant mode has been used for the observer-based controller design process, and a multi-objective genetic algorithm optimisation scheme is used to search for an optimal solution within some pre-defined constraint conditions. The best solution here is regarded as one that offers the greatest vibration mitigation performance amongst the solutions identified.

Keywords

Vibration control, state estimation, dynamic compensators, optimal

1. Introduction

The assessment of vibration serviceability performance of civil engineering structures, for example, floors and footbridges often requires some fundamental questions to be answered. For example; What are the sources of vibration? Where does the objection to excessive vibration arise from? What are the typical responses expected? (Hanagan, 2003). For these pedestrian structures, humans

[1] University of Exeter, Vibration Engineering Section, College of Engineering, Mathematics and Physical Sciences, Exeter, EX4 4QF, UK
[2] Full Scale Dynamics Limited, The Sheffield Bioincubator, 40 Leavygreave Road, Sheffield, S3 7RD, UK

Corresponding author:
Donald S Nyawako, University of Exeter, Vibration Engineering Section, College of Engineering, Mathematics and Physical Sciences, Exeter, EX4 4QF, UK
Email: D.S.Nyawako@exeter.ac.uk)

present the dominant source of excitation. Their dynamic forces from activities such as walking changes in time and space and also varies considerably not only between people of different ages, weights, stride lengths, speeds etc. but also for a single individual who often cannot repeat two identical steps (Racic et al, 2009). With typical walking frequencies ranging from 1.0 – 3.0 Hz, the walking forces also contain harmonics at these frequencies which have the potential to excite resonance in these structures.

Contemporary complaints or failures in vibration serviceability performances of the above structures is often attributed to advancements in design and materials technologies and architectural trends that result in longer span, more lightweight and open plan systems with low modal frequencies and damping ratios. For footbridges, vibration serviceability limits and loading patterns under pedestrian excitation are specified in various design guidelines: BD37/01, BS5400, HiVoSS, and Setra. In BD37/01, as an example, bridges with vertical and horizontal natural frequencies greater than 5 Hz and 1.5 Hz, respectively, are deemed to be okay. Otherwise, the limiting vibration levels are defined by $a_{max} = 0.5\sqrt{f_o}$, in which f_o is the fundamental frequency of the footbridge. As pertains to floors, there are also many guidelines (Smith et al, 2009, BS 6841, ISO 10137, BS6472) that specify desirable vibration serviceability performances. BS6472, for example, uses frequency weighted accelerations, in which there are various curves relating to permissible acceleration limits in different floors with respect to usage.

Vibration mitigation measures are often introduced either into the mainstream design phase of civil structures when vibration serviceability problems are anticipated or as a fix for an existing problem, the latter being more widespread in past studies. Amongst the measures available include passive, active, semi-active and hybrid technologies. These external devices for absorbing excessive structural vibrations vary in size, reliability, performance, installation and running costs. For footbridge structures, the use of tuned mass dampers (TMDs) is quite popular, with many trials and installations considering single and multiple units that are optimally designed to control a single or a series of problematic resonant frequencies (Carpineto et al, 2010, Bandivadekar et al, 2012, Li et al, 2010, Caetano et al, 2010). Considering a wide spectra of human loading patterns, the devices in these studies have been successfully tuned to offer desirable vibration mitigation performances amidst the challenges imposed by off-tuning.

Other studies have investigated the potential of using active vibration control (AVC) systems. For example, there have been trials with an active mass damper (AMD) system on a stress-ribbon footbridge at FEUP, Porto (Moutinho et al, 2007) for which approximately 37 % reduction in structural response to pedestrian walking induced load was achieved. There have also been comparisons of vibration mitigation performances between TMDs and AMDs in some trials (Casado et al, 2011). This study comprised of the implementations of a TMD and AMD unit in the Valladolid Science Museum footbridge in Spain. Vibration mitigation performances of between 60 - 80 % were realised for both systems. The AVC systems in both of these studies made use of the velocity feedback control scheme, for which control gains can easily be tuned. AMD units were found to be robust to off-tuning problems and single units can effectively control multiple vibration modes simultaneously. Numerous other studies can be found in the literature but only a few extracts from some case studies have been presented here. Field trials of AMD units for floor vibration control have yielded considerable

enhancement to their vibration serviceability performances (Diaz et al, 2010, Nyawako et al, 2013), with most studies implementing direct output feedback approaches like DVF. The benefits of these systems for this application is their ability to tackle a wide array of frequencies simultaneously whilst making use of much smaller units, all potentially with minimal disruptions to in-service facilities.

The use of other advanced AVC schemes like the modal control approaches in civil engineering applications has mainly been for the control of earthquake and wind excited structures. One such study comprises of the design of an optimal controller in modal space and the use of fuzzy control to tune the modal control gains (Park et al, 2004). In other studies, pole placement and optimal control (LQR, LQG) techniques have also been used (Chung et al, 1998, Wu et al, 1998) with some degree of success. Some challenges concerning design freedoms that guarantee both closed-loop stability and controller stabilities have been addressed, for example, in the works of Liu and Daley, 1998 and Liu et al, 2000 for observer-based and polynomial pole assignment controllers.

This paper focuses on suppression of human-induced vibrations in a walkway bridge using AVC. It compares vibration mitigation performances of two sets of controller schemes: (1) a proportional-integral (PI) controller based on measured walkway bridge acceleration response, and (2) a series of reduced-order observer-based (dynamic) controllers formulated from a single and three structural vibration modes, respectively, and also implemented on measured walkway bridge acceleration response. As dynamic compensator forms can have multiple solutions, depending on various choices of the plant and observer eigenvalues, a multi-objective genetic algorithm optimisation and some simulation studies are used to identify what might be regarded as the 'best' solution for these case studies. All of the controllers designed in Matlab were implemented in dSPACE hardware: ACE1103 consisting of a DS1103 PowerPC GX/1 GHz controller board and CLP1103 connector/LED panel.

2. Walkway bridge and actuator dynamics

The structure used in these studies is a walkway bridge within the Forum Building at the University of Exeter. Figure 1a shows a plan view and Figure 1b is a sectional elevation. It comprises of two 500x300x16 mm rectangular hollow section (RHS) primary beams of approximately 14.5 m and 14.7 m in length and spaced at 2.7 m centre to centre, with tapered 300x200x16 mm RHS beams welded underneath. Additionally, secondary beams of 80x80x8 mm RHS run at 1800mm centre to centre perpendicular to the primary beams. The flooring comprises a 130 mm thick concrete on RLSD Holorib S350 profiled metal deck, 0.9 mm gauge with A193 mesh. Ceramic tiles form the final floor finishing.

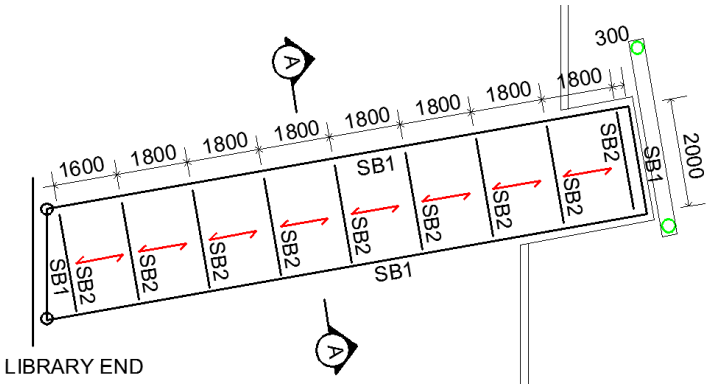

a) Plan view (dimensions in mm)

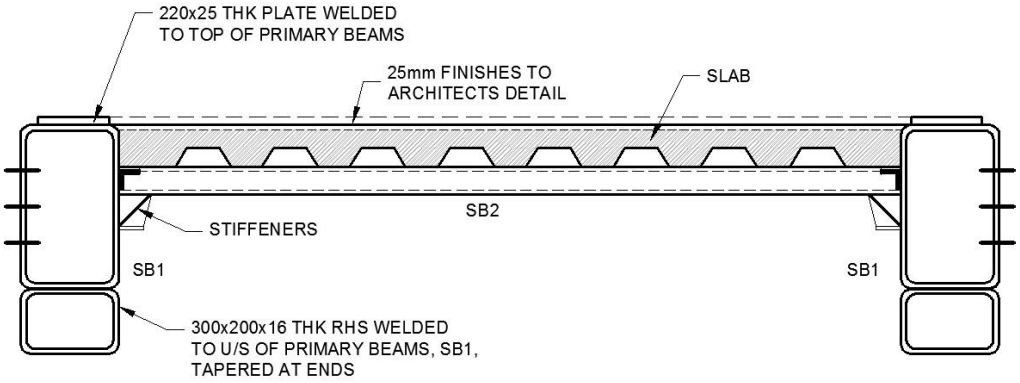

b) Section A-A

Figure 1. Walkway bridge structure in Forum building at the University of Exeter

The test grid in Figure 2 was used for the EMA to evaluate the dynamic properties of the structure. These comprised of frequency response function (FRF) measurements using an array of 13 Honeywell QA750 servo accelerometers mounted on levelled Perspex plates, and two APS Dynamics Model 400 electrodynamic shakers that were sited at TPs 4 and 7. The shakers were driven by statistically uncorrelated random signals and their forces were measured using Endevco 7754A-1000 accelerometers that were attached to the inertial masses. As there were more test points than accelerometers, it was necessary to use roving response measurements; the shakers were left in position and served as references whilst the accelerometers were roved along grid lines 1-13, 14-26 and 27-39. Data acquisition was carried out using a Data Physics Mobilyzer II digital spectrum analyser. The force and vibration response data were sampled using a baseband setting of 80 Hz on the spectrum analyser. Each data acquisition window was 32s in length, and the acquisitions were made using a Hanning window and 75% overlap, which were averaged to calculate the uncontrolled FRFs.

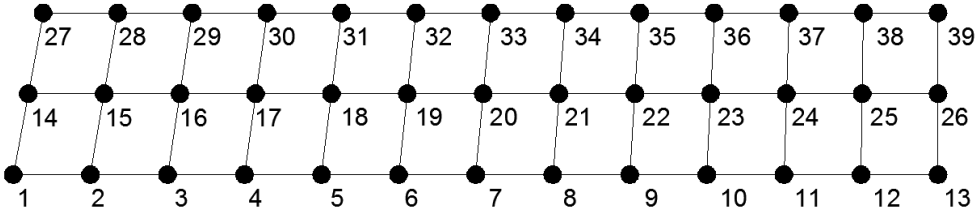

Figure 2. Test grid for modal testing

The point accelerance FRF measurements at TPs 4 and 7 (magnitude and phase) are shown in Figures 3a and 3b. The FRF data from all excitation and response points were analysed using the ME'scopeVES parameter estimation software to determine the modal properties of the walkway bridge, i.e. the natural frequencies, modal damping ratios and mode shapes. The key results of the modal parameter estimation are summarised in Table 1.

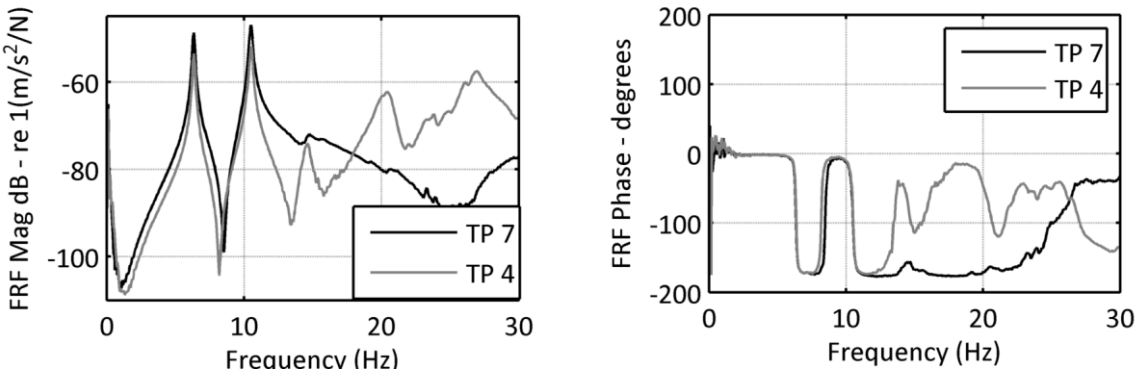

a) FRF Magnitude – TPs 4 and 7 b) FRF Phase – TPs 4 and 7

Figure 3. FRF Magnitude and Phase at TPs 4 and 7

Table 1. Summary of estimated modal properties from EMA

Mode	Natural Frequency [Hz]	Damping Ratio [%]
1	6.34	1.0
2	10.5	0.9
3	14.6	2.2
4	20.5	2.6
5	26.1	0.7
6	26.9	1.1
7	34.3	2.3

TP7 is selected for siting an actuator and sensor pair in the AVC studies in this work as it is close to the antinode of the two lowest modes of vibration that are prone to excitation from walking. The transfer function at TP7 for controller design, considering the 'approximate' collocated case between the acceleration (output) and the force (input) is obtained in the Laplace domain using the modal expansion approach in Equation 1. This comprises of a finite set of modes within the frequency bandwidth of interest. $\mu_i \geq 0$ is the inverse of the 'effective mass' corresponding to TP7, ζ_i is the modal damping ratio and ω_i is the modal frequency, all being associated with the mode i.

$$G_p(s) = \sum_{i=1}^{n} \frac{\mu_i s^2}{s^2 + 2\zeta_i \omega_i s + \omega_i^2} \quad (1)$$

The actuators used in this research work are APS dynamics, model 400 electro-seis shakers. They have an inertial mass of 30.4 kg and a maximum stroke of 15 cm. The peak drive voltage to the shaker amplifier, APS Dynamics Model 124-EP, is 2.0 V. Figures 4a and 4b show the experimental force-voltage characteristics for the current drive mode in which the actuators are used here, within the frequency span 0 - 40 Hz. Also within these plots are the traces of the derived analytical model in Equation 2a, with parameters determined as: K_{act} = 300 N/V, ζ_{act} = 0.10 and ω_{act} = 8.17 rad/s. Equation 2b shows the displacement-voltage (m/V) characteristic, and K_{act_d} = 10.

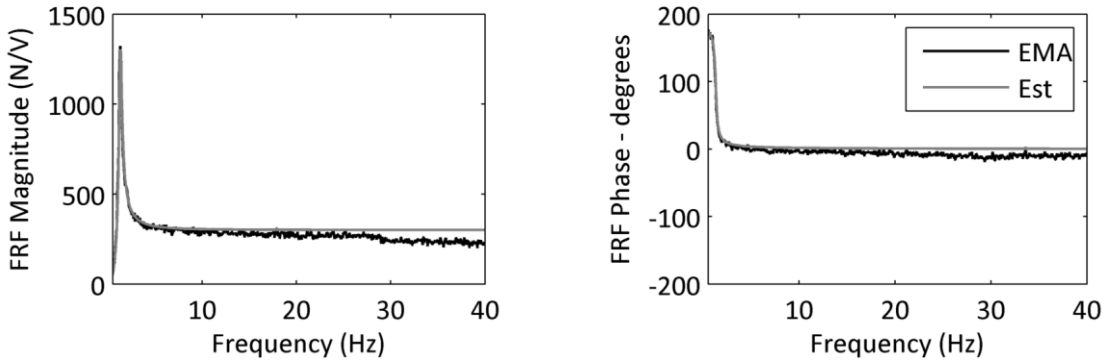

a) FRF Magnitude b) FRF Phase

Figure 4. Actuator dynamics – FRF magnitude and phase (EMA – experimentally measured trace, Est –analytically derived trace)

$$G_{act}(s) = \frac{F(s)}{V(s)} = \frac{K_{act}s^2}{s^2 + 2\zeta_{act}\omega_{act}s + \omega_{act}^2} \tag{2a}$$

$$G_{act\_d}(s) = \frac{D(s)}{V(s)} = \frac{K_{act\_d}}{s^2 + 2\zeta_{act}\omega_{act}s + \omega_{act}^2} \tag{2b}$$

3. Controller schemes

Two controller schemes are selected for the studies presented here. They include:

a) A proportional-integral (PI) controller on measured structural acceleration – this optimizes the controller to derive benefits of DVF at low frequency and those of direct acceleration feedback at higher frequencies.
b) A series of observer-based (dynamic) controllers – these are designed to meet various design objectives, which include both global control (the control of all structural resonant frequencies observable) and targeted control (isolation and control of specific resonant frequencies).

TP 7 in Figure 2 that captures the two lowest vibration modes of the walkway bridge that are prone to pedestrian excitation is used for siting the collocated sensor and actuator pair.

The PI controller takes the form of Equation 3, in which K_g, a_1 and b_1 are the compensator, $G_c(s)$, parameters to be evaluated. It can be assumed that $b_1 = 1$. As noted above, the addition of the proportional term to the integral term is mainly to enhance the vibration mitigation performance of the PI controller over a broader frequency bandwidth as well as offering better stability margins.

$$G_c(s) = G_{pi}(s) = K_g\left(\frac{a_1 s + b_1}{s}\right) \tag{3}$$

Observer-based controller sets, $G_c(s)$, are designed from Figure 5 below and considering reduced order walkway bridge models from Equation 1 for $i = 1$ and $i = 3$. From Figure 5, (A_p, B_p, C_p) and (A_{po}, B_{po}, C_{po}) are the existing walkway bridge dynamics and its reduced-order model (ROM). $\hat{x}$ are estimated modal states of the observer, K_p are the modal feedback gains required to achieve desired closed-loop eigenvalues of the walkway bridge and K_e are the observer gains.

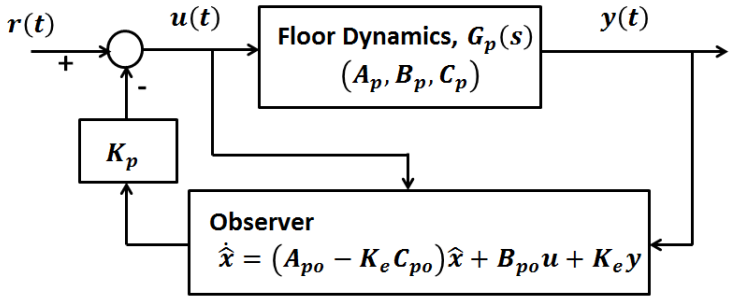

Figure 5. Shortened form of dynamic regulator (Xue et al, 2002)

The feedback signal $K_p\hat{x}(t)$ is driven by $u(t)$ and $y(t)$ in Equations 4 and 5. $\hat{x}_1(t)$ and $\hat{x}_2(t)$ are only used to distinguish modal states driven by $u(t)$ and $y(t)$. These are expressed in the Laplace domain as the two subsystems $H_u(s)$ and $H_y(s)$ in Equations 6 and 7. Equation 8 shows the resultant dynamic controller from merging these two equations. From Equation 1, for n = 1 and n = 3, the controller orders evolve as shown in Equations 9a and 9b. k_{ij}, α_{ij} and β_{ij} represent the compensator coefficients. Checks are made to ensure the controllability, Q_c, and observability, Q_o, matrices in Equations 10a and 10b have full rank.

$$\dot{\hat{x}}_1(t) = (A_{po} - K_e C_{po})\hat{x}_1(t) + B_{po}u(t) \qquad y_{a1}(t) = K_p\hat{x}_1(t) \tag{4}$$

$$\dot{\hat{x}}_2(t) = (A_{po} - K_e C_{po})\hat{x}_2(t) + K_e y(t) \qquad y_{a2}(t) = K_p\hat{x}_2(t) \tag{5}$$

$$H_u(s) = \frac{Y_{a1}(s).\hat{X}_1(s)}{\hat{X}_1(s).U(s)} = K_p\big(sI - (A_{po} - K_e C_{po})\big)^{-1}B_{po} \tag{6}$$

$$H_y(s) = \frac{\hat{X}_2(s).Y_{a2}(s)}{Y(s).\hat{X}_2(s)} = K_p\big(sI - (A_{po} - K_e C_{po})\big)^{-1}K_e \tag{7}$$

$$G_c(s) = \frac{H_y(s)}{1 + H_u(s)} \tag{8}$$

$$G_{c1}(s) = \frac{k_{11}(s + \alpha_{11})}{(s^2 + \beta_{11}s + \beta_{21})} \tag{9a}$$

$$G_{c3}(s) = \frac{k_{13}(s + \alpha_{13})(s^2 + \alpha_{23}s + \alpha_{33})(s^2 + \alpha_{43}s + \alpha_{53})}{(s^2 + \beta_{13}s + \beta_{23})(s^2 + \beta_{33}s + \beta_{43})(s^2 + \beta_{53}s + \beta_{63})} \tag{9b}$$

$$Q_c = \left[B_{po} \;\; A_{po}B_{po} \;\; A_{po}^2B_{po} \;\cdots\; A_{po}^{n-1}B_{po}\right] \tag{10a}$$

$$Q_o = \left[C_{po} \quad C_{po}A_{po} \quad \cdots \quad C_{po}A_{po}^{n-1}\right]^T \tag{10b}$$

Figure 6 shows the control scheme for implementation of the above controller schemes. $G_p(s)$, $G_{act}(s)$, $G_{bp}(s)$, $G_{not}(s)$ and $G_c(s)$ are the walkway bridge, actuator, band pass filter, notch filter and controller dynamics. For mitigation of human induced vibrations, the disturbance rejection property in Equation 11 is the key objective as human walking forces cannot directly be measured.

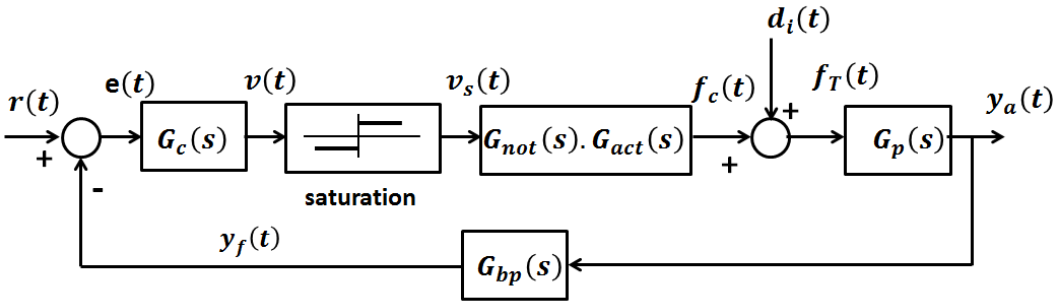

Figure 6. Controller scheme for both PI controller and observer based controller

$$Y_a(s) = \frac{G_p(s)}{1 + G_p(s)G_{not}(s)G_{act}(s)G_c(s)G_{bp}(s)} D_i(s) \tag{11}$$

Equation 12 shows the transfer function between the actuator displacement and the disturbance input. This is used to study the sensitivity of the actuator reactive mass displacement to the disturbance input mainly around the actuator resonant frequency which, coincidentally falls within the range of human walking frequencies. Notch filters in Equation 13 ($k_{not} > 1$) are designed to compensate for the low damping of the actuator in the current drive mode and thereby reduce the above sensitivity. $G_{act\_d}(s)$ is given in Equation 2b.

$$Y_{act\_d}(s) = -\frac{G_{not}(s)G_{act\_d}(s)G_c(s)G_{bp}(s)G_p(s)}{1 + G_{not}(s)G_{act\_d}(s)G_c(s)G_{bp}(s)G_p(s)} D_i(s) \tag{12}$$

$$G_{not}(s) = \frac{s^2 + 2\zeta_{not}\omega_{not}s + \omega_{not}^2}{s^2 + 2k_{not}\zeta_{not}\omega_{not}s + \omega_{not}^2} \tag{13}$$

4. Controller parameters and analytical and experimental studies

The governing requirements to be met by all controllers are set out as:

a) To meet minimum stability margins, i.e. Gain Margin of 3dB and Phase Margin of 30 degrees.
b) The peaks of Equation 12 around the actuator resonance, i.e. $s = j\omega_{act}$, should not exceed the threshold of 8 mm/N. This is a dynamic quantity that reduces the potential for stroke saturation from the harmonics of walking around the actuator resonant frequency.

The optimum PI controller here is defined by the maximum gain achievable without exceeding condition (b) above, since the minimum stability margins requirements for condition (a) are met as shown in Table 2. The design here comprises of inclusion of a notch filter with parameters in Equation 13 chosen as: $\omega_{not} = 8.2$ rad/s, $k_{not} = 5.2$, and $\zeta_{not} = 0.12$. A second order Butterworth band pass filter with cut-off frequency 1.0 – 27.5 Hz is also implemented and saturation voltage is set to 2.0 V. This yields $K_g = 900$, $a_1 = 0.0025$ and $b = 1.0$ in Equation 3. Figures 7a, 7b and 7c show a root locus plot of the closed-loop system in Figure 6, the Nyquist contour of $G_{pi}(s)G_{act}(s)G_{not}(s)G_{bp}(s)G_p(s)$, and a trace of the absolute value of the actuator displacement to disturbance input force within the critical frequency span 0 – 6 Hz, i.e. around the actuator resonant frequency. The traces labelled (A)

and (E) in Figure 7b represent the ROM and EMA measurement at TP7. In Figure 7c, PI – A, PI – E and PI – Comp A, PI – Comp E refer to the closed-loop systems without and with notch filter inclusion for the analytical and experimental traces. It highlights the need for inclusion of the notch filter to satisfy requirement (b) above. Figures 9a and 9b show the magnitude and phase plots of the band pass, G_{bp1}, and notch filter, G_{not1}, implemented with the PI controller.

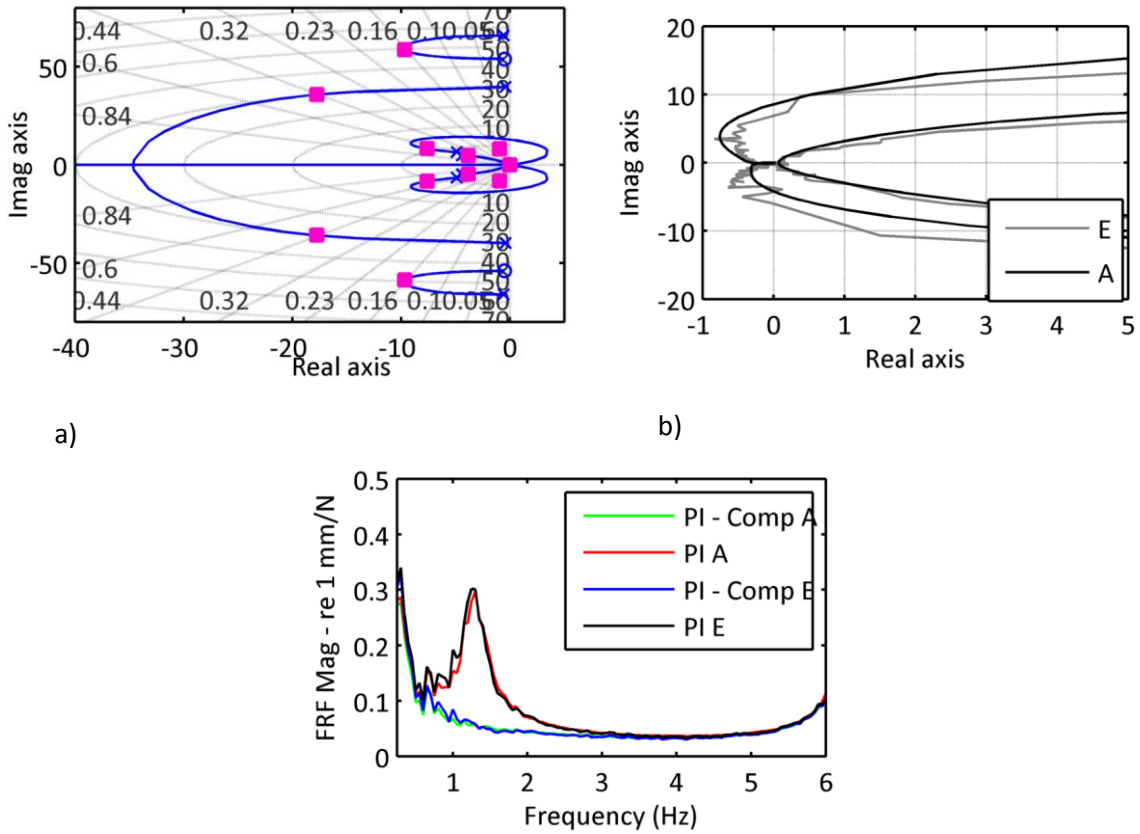

a) b)

c)

Figure 7. (a) Root locus plot. (b) Nyquist contour of $G_{pi}(s)G_{act}(s)G_{not}(s)G_{bp}(s)G_p(s)$. (c) Actuator displacement to input force characteristic in Equation 12 with PI controller

The acronyms PP are used to refer to the observer-based compensator sets. Desired closed-loop eigenvalues of selected modes of vibration are chosen using the gain terms in Table 3. Using PP1 as an example, it is desired to have a closed-loop damping of $k_{zeta1} * zeta1$, where $zeta1$ is the open-loop damping of mode 1. PP1 takes the form of Equation 9a, whilst PP2, PP3 and PP4 all take the form of Equation 9b. The observer-based compensators, $G_{c1}(s), G_{c2}(s), G_{c3}(s)$ and $G_{c4}(s)$ in Equations 14a to 14d are designed to realise the design objectives set out in Table 3 for PP1, PP2, PP3 and PP4.

$$G_{c1}(s) = \frac{677.5(s+6.8)}{(s^2+24.6s+107.7)} \tag{14a}$$

$$G_{c2}(s) = \frac{386.6(s+622.7)(s^2+3.5s+4368)(s^2+11.3s+4.6e4)}{(s^2+155.4s+4134)(s^2+16.8s+4174)(s^2+49.3s+5.6e4)} \tag{14b}$$

$$G_{c3}(s) = \frac{276.7(s+1111)(s^2+4.1s+1604)(s^2+11.3s+4.6e4)}{(s^2+10.8s+1560)(s^2+154.3s+8130)(s^2+51.9s+5.6e4)} \tag{14c}$$

$$G_{c4}(s) = \frac{627.3(s+598.2)(s^2+23.5s+2688)(s^2+11.3s+4.6e4)}{(s^2+37.9s+1772)(s^2+157.6s+8849)(s^2+49.2s+5.5e4)} \quad (14d)$$

$G_{c1}(s)$ possess lossy-integrator type characteristics and attenuates both the first and second modes of vibration. $G_{c2}(s)$ is designed to isolate and control mainly the first vibration mode, $G_{c3}(s)$ is designed to isolate and control mainly the second vibration mode, whilst $G_{c4}(s)$ is designed to control both the first and second vibration modes of the walkway bridge. All the compensators are closed-loop stable and Figure 8 shows their FRF magnitude and phase characteristics. A second order Butterworth band pass filter, G_{bp2}, with cut-off frequency 0.75 – 28.5 Hz in Figure 9a is included with all the dynamic compensators to prevent potential spillover from higher frequencies. A notch filter, G_{not2}, in Figure 9b with parameters optimised at $\omega_{not} = 8.2\ rad/s$, $k_{not} = 1.6$, and $\zeta_{not} = 0.12$ ensures requirement (b) above is met. The minimum stability margins with implementations of these controllers in Figure 6 is shown in Table 2. Desired and the achieved closed-loop eigenvalues with these observer-based controllers are reflected in Table 3.

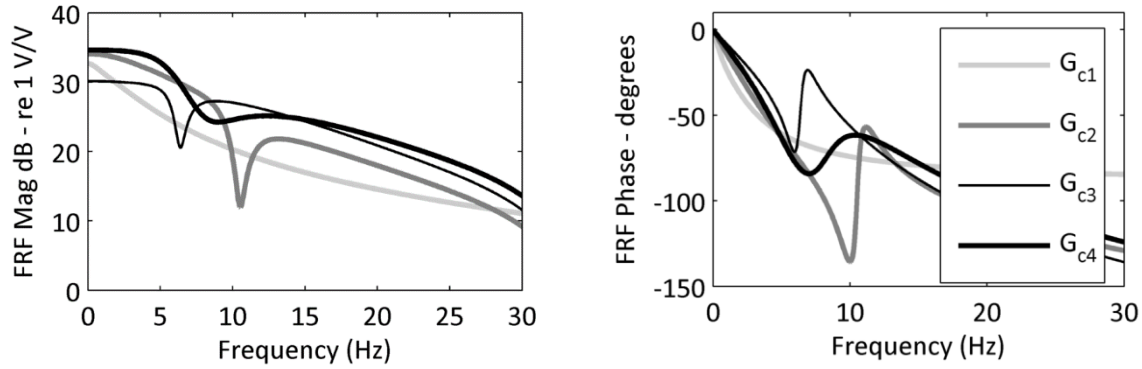

a) FRF Magnitude b) FRF Phase

Figure 8. Compensator magnitudes and phases: $G_{c1}(s), G_{c2}(s), G_{c3}(s), G_{c4}(s)$

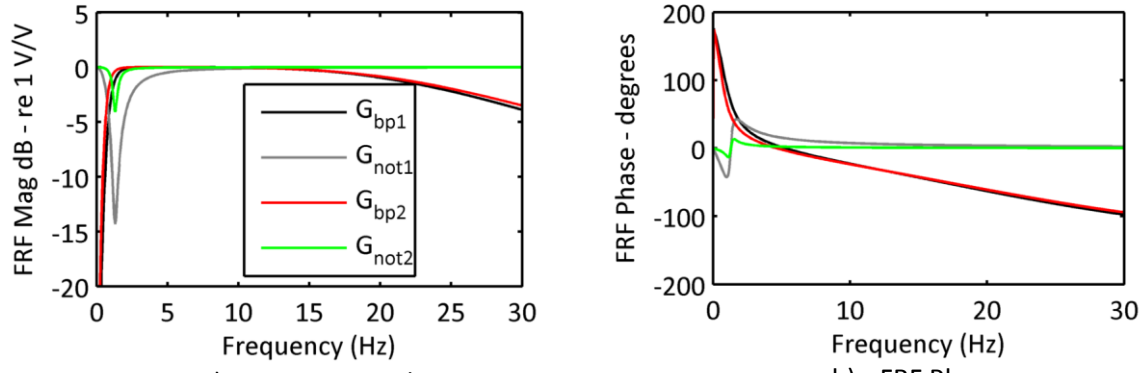

a) FRF Magnitude b) FRF Phase

Figure 9. Band pass and Notch filter magnitudes and phases for PI and PP compensators (subscripts 1 refer to PI controller and subscripts 2 refer to PP controllers)

Root locus plots, Nyquist contour plots of $G_c(s)G_{act}(s)G_{not}(s)G_{bp}(s)G_p(s)$, and traces of the absolute values of the actuator displacement to disturbance input force relationships similar to those in Figure 7 can also be derived for the reduced order observer controllers. These are, however, not shown here.

Table 2. Stability margins and displacement-force characteristics for all controllers

Controller	GM - dB	PM - degrees	Displacement to input force ratio around actuator resonance (mm/N)
$G_{pi}(s)$	9.8	58.5	0.080
$G_{c1}(s)$	14.3	59.1	0.075
$G_{c2}(s)$	10.9	52.7	0.070
$G_{c3}(s)$	9.5	42.6	0.060
$G_{c4}(s)$	9.5	43.1	0.075

Table 3. Desired and achieved eigenvalues of modes 1 and 2 of the walkway bridge structure

		Gain parameters	Desired closed-loop eigenvalues	Achieved closed-loop eigenvalues
PP1	Mode 1	$k_{zeta1} = 25.5$	$-11.2 \pm 39.2i$	$-10.5 \pm 33.9i$
PP2	Mode 1	$k_{zeta1} = 16.5$	$-7.4 \pm 40.2i$	$-7.7 \pm 38.1i$
	Mode 2	$k_{zeta2} = 2.5$	$-1.5 \pm 65.9i$	$-1.4 \pm 66.2i$
	Mode 3	$k_{zeta3} = 1.0$	$-5.6 \pm 215.4i$	$-5.6 \pm 215.4i$
PP3	Mode 1	$k_{zeta1} = 5.5$	$-1.9 \pm 40.7i$	$-1.3 \pm 40.2i$
	Mode 2	$k_{zeta2} = 15.5$	$-9.0 \pm 62.0i$	$-7.0 \pm 60.1i$
	Mode 3	$k_{zeta3} = 1.0$	$-5.6 \pm 215.4i$	$-5.6 \pm 215.4i$
PP4	Mode 1	$k_{zeta1} = 16.5$	$-9.9 \pm 56.8i$	$-8.8 \pm 58.8i$
	Mode 2	$k_{zeta2} = 17.5$	$-8.0 \pm 48.9i$	$-6.9 \pm 46.0i$
	Mode 3	$k_{zeta3} = 1.0$	$-5.6 \pm 215.4i$	$-5.6 \pm 215.4i$

The disturbance rejection results from the analytical studies and experimental implementation of all the controller schemes are presented in Figures 10 and 11, and Table 4 highlights the attenuations in the two lowest vibration modes.

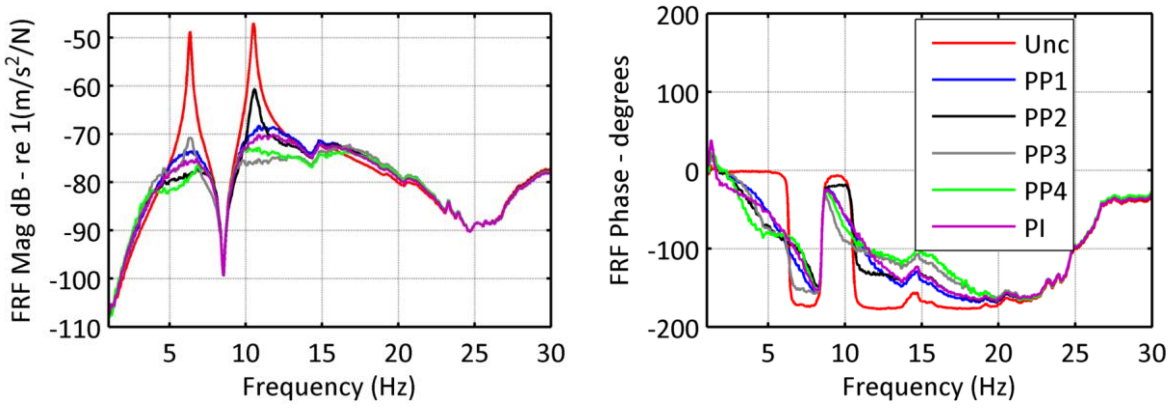

a) b)

Figure 10. Uncontrolled and controlled frequency response functions for all controllers (analytical)

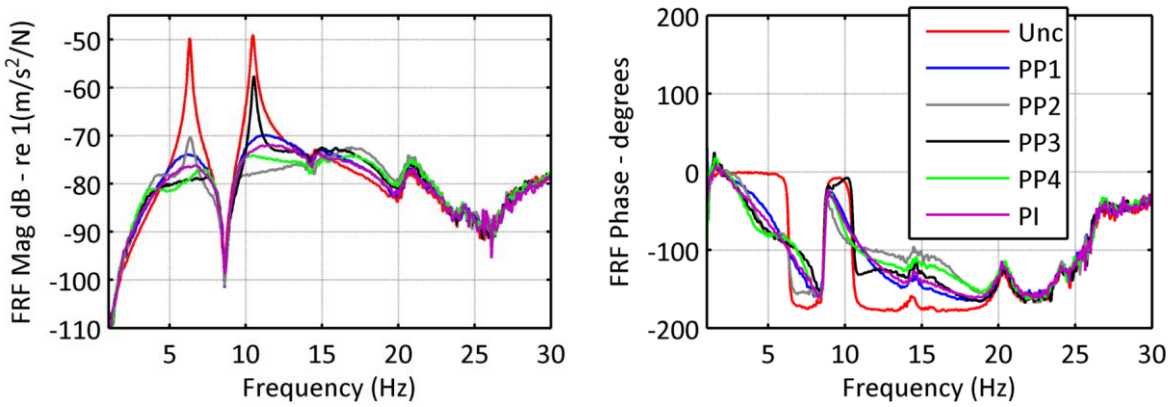

a) b)

Figure 11. Uncontrolled and controlled frequency response functions for all controllers (experimental)

Table 4. Attenuations in target modes of vibration for all controllers

Controller	Predicted attenuations (dB)		Experimental attenuations (dB)	
	Mode 1	Mode 2	Mode 1	Mode 2
$G_{pi}(s)$	26.4	23.1	26.4	23.1
$G_{c1}(s)$	24.4	21.4	24.4	21.4
$G_{c2}(s)$	29.5	12.8	29.5	12.8
$G_{c3}(s)$	21.1	29.5	21.1	29.5
$G_{c4}(s)$	28.5	26.8	28.5	26.8

No spillover effects from higher frequencies was observed in the experimental implementation of the observer-based controllers as they possess desirable roll-off characteristics as seen in Figure 8 and the use of second order Butterworth band pass filters, that were implemented with all compensators.

The PI controller targets all structural resonant frequencies within a broad frequency bandwidth. $G_{c1}(s)$, designed based on only a single plant mode defaults to a second order controller with lossy integrator type characteristics and also targets all structural frequencies within a given bandwidth. The dynamic compensators, $G_{c2}(s), G_{c3}(s), G_{c4}(s)$, are of sixth order by virtue of the use of three plant modes for their design and there is an increase in the design freedom to isolate and target specific resonant frequencies within a given bandwidth as can be seen in Figures 10 and 11.

The question now arises as to what might be regarded as an optimal solution to a given problem. In this work, it appears there may be numerous possible compensator solutions from different choices of desired closed-loop plant properties and observer eigenvalues, even for the most basic controller in Equation 9a. The next section deals with an optimisation scheme that is formulated to select appropriate dynamic controller parameters within a given search space that is obtained from various choices of plant closed-loop and observer eigenvalues. The optimization scheme here focuses on the dynamic compensators derived from the use of only a single plant mode for their design i.e. second order compensator types in Equation 9a.

5. Optimisation schemes

The dynamic compensators designed in the previous section are seen to offer desirable disturbance rejection properties as seen in Figures 10 and 11. In Table 4, this subsequently translates to impressive attenuations in the walkway bridge responses under human-induced vibrations. It is now desirable to determine an optimal solution within some defined scope and a particular approach is pursued here. As seen previously, the selection of desired closed-loop eigenvalues of the walkway bridge structure and appropriate observer eigenvalues results in plant and observer gains, K_p and K_e, that are used in the formulation of the dynamic compensator, $G_{c1}(s)$ in Equations 9a,14a. This equation comprises of real gains k_{11}, α_{11}, β_{11} and β_{22}. Multiple gain sets, K_p and K_e, can be obtained from the pre-selection of various closed-loop plant eigenvalues and associated observer eigenvalues, and these ultimately result in multiple sets of parameters k_{11}, α_{11}, β_{11} and β_{22}. An example of this is demonstrated here, where only the first plant mode is used for the dynamic controller design.

Some desired closed-loop eigenvalues of the first vibration mode of the walkway structure can be selected as shown in Table 5, following a similar procedure to that in Table 3. Appropriate eigenvalues of the observers are also determined. The resulting closed-loop eigenvalues of the first mode of vibration are also provided. The coefficients of $G_c(s)$, of form in Equations 9a,14a, for the various compensators in Table 5 are shown in Table 6. Root locus plots, Nyquist contour plots of $G_c(s)G_{act}(s)G_{not}(s)G_{bp}(s)G_p(s)$, and traces of the absolute values of the actuator displacement to disturbance input force relationships similar to those in Figure 7 can also be developed with these reduced order observer controllers: PP1-1 to PP1-7. These are, however, not shown here. Figure 12 shows typical closed-loop FRFs for closed-loop systems with three of the compensators in Table 6, reflecting many potential choices, again with these quick iterations.

Table 5. Desired eigenvalues of mode 1, realised and enhanced eigenvalues of Walkway Bridge

Controller	Desired closed-loop eigenvalues	Observer eigenvalues	Achieved closed-loop eigenvalues
PP1 – 1	$-11.9 \pm 45.2i$	$-16, -2$	$-12.2 \pm 42.4i$
PP1 – 2	$-4.0 \pm 40.2i$	$-6.0 \pm 8.0i$	$-4.0 \pm 39.2i$
PP1 – 3	$-2.7 \pm 40.1i$	$-4.1 \pm 5.6i$	$-2.6 \pm 39.3i$
PP1 – 4	$-1.7 \pm 40.2i$	$-4.7 \pm 6.4i$	$-1.8 \pm 39.7i$
PP1 – 5	$-6.5 \pm 41.4i$	$-7.8 \pm 1.7i$	$-6.7 \pm 39.1i$
PP1 – 6	$-3.1 \pm 40.0i$	$-2.1 \pm 3.4i$	$-3.5 \pm 38.9i$
PP1 – 7	$-3.3 \pm 39.9i$	$-3.7 \pm 5.9i$	$-3.2 \pm 39.1i$

Table 6. Optimal controller parameters of $G_{c1}(s)$ in Equation 13a corresponding with selected closed-loop eigenvalues

Gain parameters				
Controller	k_{11}	α_{11}	β_{11}	β_{21}
PP1 – 1	392.5	65.0	39.6	415.6
PP1 – 2	239.1	20.2	18.9	182.8
PP1 – 3	162.8	16.0	12.9	87.2
PP1 – 4	91.8	28.2	12.0	86.4

PP1 – 5	344.8	36.0	27.8	251
PP1 – 6	225.7	9.3	9.6	40.7
PP1 – 7	200.7	12.9	12.8	89.8

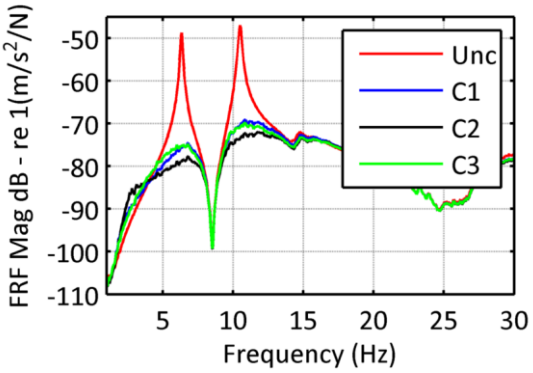

Figure 12. Typical closed-loop FRFs

By making use of the coefficients derived in Table 6, a search space is proposed as shown in the pole-zero maps in Figure 13. This is unique to the present work. The question that arises now is how to derive an optimal controller gain solution within this search space. This is addressed in this paper using a multi-objective genetic algorithm (GA) optimisation scheme. Equation 9a can be re-expressed as shown in Equation 15. Table 7 highlights the selected envelopes of the compensator coefficients for the present study which would provide a solution that lies within this search space. These are minimum and maximum values from the gain parameters in Table 6.

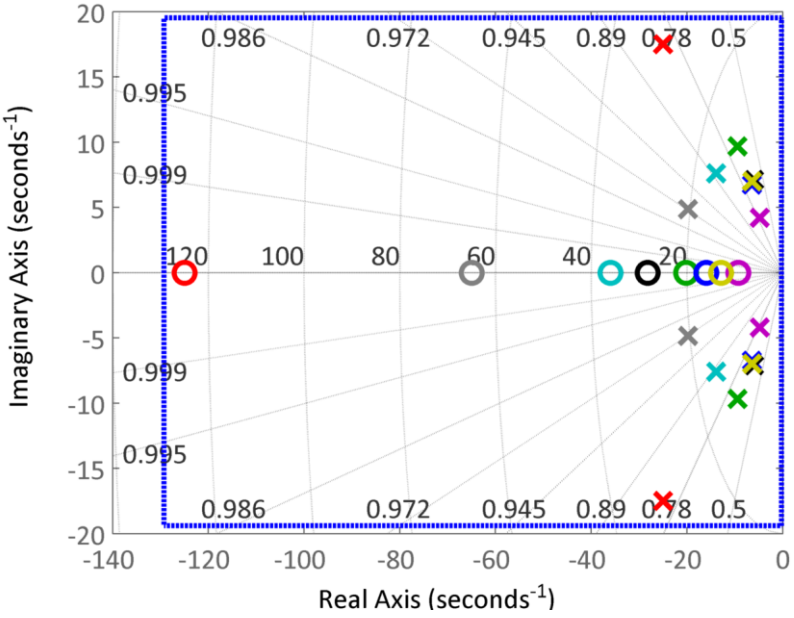

Figure 13. Pole-zero maps of the compensators in Table 6

$$G_{c1}(s) = \frac{k_{11}(s+\alpha_{11})}{(s^2+\beta_{11}s+\beta_{21})} = \frac{k_{11}s+k_{21}}{(s^2+\beta_{11}s+\beta_{21})} \quad (15)$$

Table 7. Selected envelopes of coefficients $k_{11},\ k_{21},\ \beta_{11},\ \beta_{21}$

Parameter	$\boldsymbol{k_{11}}$	$\boldsymbol{k_{21}}$	$\boldsymbol{\beta_{11}}$	$\boldsymbol{\beta_{21}}$
Min.	400	9000	9	30
Max.	1000	50000	50	450

This is a nonlinear programming problem in which the objective function and most of the constraint conditions are nonlinear functions of the design variables. The multi-objective optimization problem is set out as the minimization of the objective function in Equation 16, i.e. the disturbance rejection property, whose magnitude and phase properties are considered over the entire frequency bandwidth, $\omega_i\ , i = 1,2,\dots,n,\ s = j\omega$. This represents the frequency range 0.5 – 80.0 Hz in this work. $G_c(j\omega_i) = f\{k_{11}, k_{21}, \beta_{11}, \beta_{21}\}$ is the only variable which represents the controller term whose gain parameters are to be determined from the envelopes outlined in Table 6. The aim of the objective function in Equation 16 is to attenuate the resonant peaks of the dominant frequencies whilst realising a bounded closed-loop solution of Equation 11 over the frequency bandwidth of interest noted above subject to some constraint terms which are introduced. This also aims to mitigate the potential for spill over instabilities over the frequency range of interest to be controlled. The non-linear constraint conditions are set out in Equations 17 to 22 and explained.$G_{pd}(j\omega_i)$ in Equation 17 is a desired closed-loop trace.

Objective function: minimize

$$H_c(j\omega_i) = \frac{G_p(j\omega_i)}{1 + G_p(j\omega_i)G_{bp}(j\omega_i)G_{not}(j\omega_i)G_{act}(j\omega_i)\boldsymbol{G_c}(j\omega_i)}\ , \quad i = 1,2,\dots,n \quad (16)$$

Subject to constraint conditions:

$$|H_c(j\omega_i)| \le \left|G_{pd}(j\omega_i)\right| - |\varepsilon|\ , i = 0,1,2,\dots,n \quad (17)$$

$$k_{1L} \le k_{11} \le k_{1U}, \qquad k_{2L} \le k_{21} \le k_{2U} \quad (18)$$

$$\beta_{1L} \le \beta_{11} \le \beta_{1U}, \qquad \beta_{2L} \le \beta_{22} \le \beta_{2U} \quad (19)$$

$$\max\left\{-\text{real}\left(\text{Nyquist}\left(G_p(j\omega_i)G_{bp}(j\omega_i)G_{act}(j\omega_i)G_{not}(j\omega_i)\boldsymbol{G_c}(j\omega_i)\right)\right)\right\} \le 1.0 \quad (20)$$

$$\frac{k_1\alpha_{11}}{k_1} > 0.5\beta_{11} + 0.5 * \text{abs}\left(\text{sqrt}(\beta_{11}\beta_{11} - 4\beta_{21})\right) \quad (21)$$

$$\left|\frac{G_p(j\omega_i)G_{bp}(j\omega_i)G_{not}(j\omega_i)G_{actd}(j\omega_i)\boldsymbol{G_c}(j\omega_i)}{1 + G_p(j\omega_i)G_{bp}(j\omega_i)G_{not}(j\omega_i)G_{actd}(j\omega_i)\boldsymbol{G_c}(j\omega_i)}\right| \le \mu_1 \quad (22)$$

Equation 17 aims to enforce the disturbance-rejection solution in Equation 11, i.e. the magnitude of the closed-loop FRF with the optimised gains to be bounded within the desired closed-loop trace, $G_{pd}(j\omega_i)$, thus mitigating potential for out-of-bounds resonances. Equations 18 and 19 are the search spaces for the controller gain parameters in Table 7. Equation 20 is formulated to ensure the Nyquist contour of the closed-loop system for the optimized controller gains does not encircle the -1 point in the s-plane and Equation 21 aims to maintain similar pole-zero maps of the resultant dynamic controller to those in Figure 16. This ensures appropriate interlacing properties within the closed-loop root locus for this case study and thereby meeting appropriate closed-loop stability properties for the selected dynamic controller coefficients. The constraint condition introduced in Equation 22 ensures that the actuator displacement to disturbance input relationship remains bounded and thus prevents potential for stroke saturation instability under pedestrian excitation. μ_1 is set to 0.08 mm/N.

The 'optimal' dynamic compensator characteristics are determined using the 'gamultiobj' multiobjective optimization function within the optimization toolbox using a GA search. These are based on the objective function and constraint conditions given in equations 16-22. With higher penalty functions, this yields 20 solutions of compensator coefficients that satisfy the constraint conditions in Equations 17-22. Figures 14a and 14b show the typical pole-zero plots of the derived compensators, in which the solutions are now less-sparse than those from the iterative studies in Figure 13.

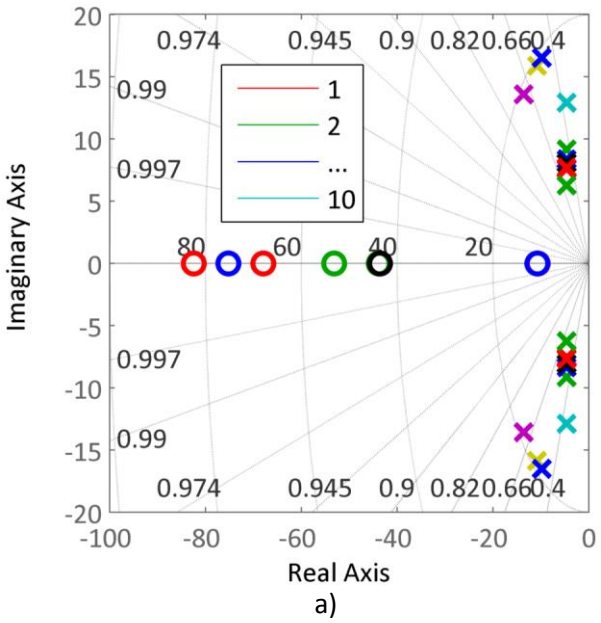

a)

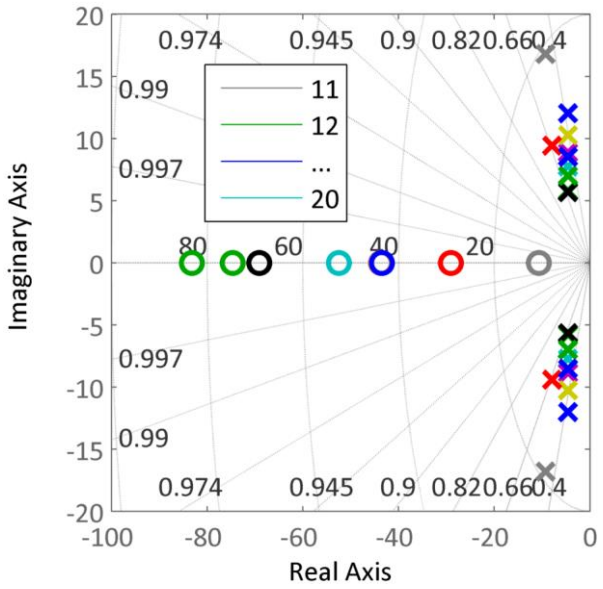

Figure 14. Pole-zero maps of the optimal compensators from the multi-objective optimisation procedure

Analytical simulations of controlled walkway responses under a synthesized walking force time history in Figure 15a (the associated Fourier spectrum of this force is also shown in Figure 15b) are then used to select a robust controller from all the sets of 'optimal' dynamic compensators in Figure 14. This is considered as a dynamic controller that offers maximum attenuation of the structural acceleration response under this synthesized pedestrian excitation force whilst satisfying desired stability margins. A typical example of uncontrolled and controlled response time histories, weighted using the BS6841 Wb weighting function (BSI, 1987), from the simulation studies are shown in Figure 16. Also shown within these plots are the 1s running RMS acceleration responses. The peaks of the 1s RMS acceleration responses from the implementation of all the controllers arising from the multi-objective optimisation process are shown in Table 8. The peaks of the running RMS acceleration responses are defined as the Maximum Transient Vibration Value (MTVV) following the recommendation of ISO 2631:1997. The MTVV of the uncontrolled response is 0.1399 m/s^2. From Table 8, vibration attenuations of between 88.1% - 92.9% are predicted for all the controllers. A typical controlled FRF trace for the derived optimal compensator 10 in Table 8 is shown in Figure 17. The control efforts from these simulation studies were pretty similar.

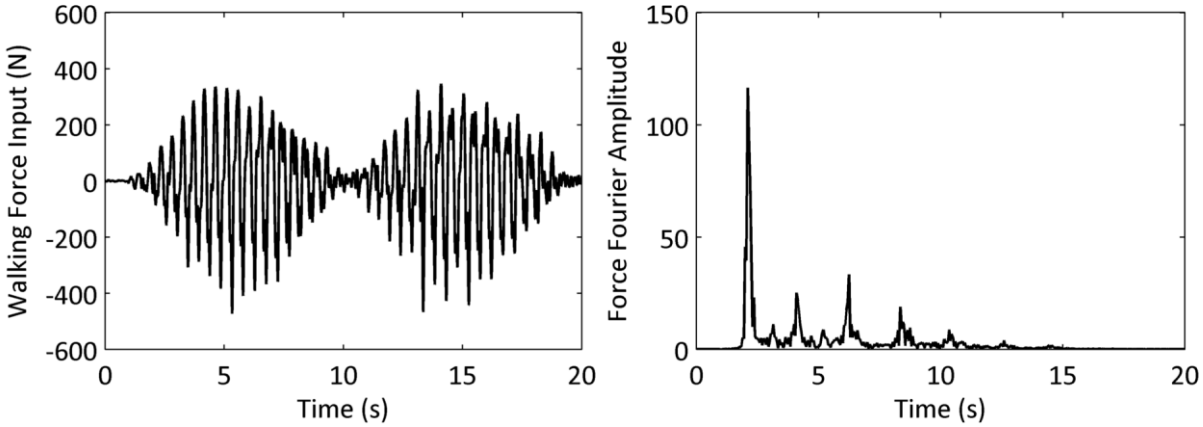

a) b)

Figure 15. (a) Synthesized walking time history for use in analytical simulations and (b) associated Fourier spectrum

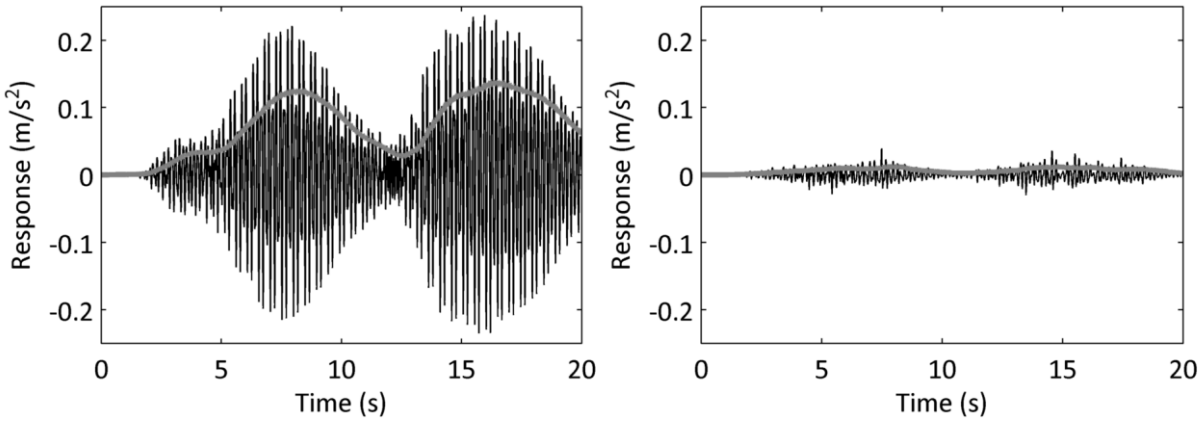

a) b)

Figure 16. Typical (a) uncontrolled and (b) controlled walking time histories

Table 8. Peak of 1s running RMS (MTVV) for BS6841 weighted controlled walking responses and percentage reductions from uncontrolled case

Compensator	**MTVV value (m/s^2)**	**% reductions**	**Compensator**	**MTVV value (m/s^2)**	**% reductions**
Uncontrolled	0.1399		PI controller	0.0120	91.4
PP 1	0.0139	90.0	PP 11	0.0100	92.9
PP 2	0.0133	90.5	PP 12	0.0145	89.6
PP 3	0.0142	89.9	PP 13	0.0159	88.6
PP 4	0.0167	88.1	PP 14	0.0123	91.2
PP 5	0.0116	91.7	PP 15	0.0119	91.5
PP 6	0.0120	91.4	PP 16	0.0120	91.4
PP 7	0.0112	92.0	PP 17	0.0145	89.6
PP 8	0.0129	90.8	PP 18	0.0104	92.6
PP 9	0.0124	91.1	PP 19	0.0131	90.6
PP 10	0.0104	92.6	PP 20	0.0123	91.2

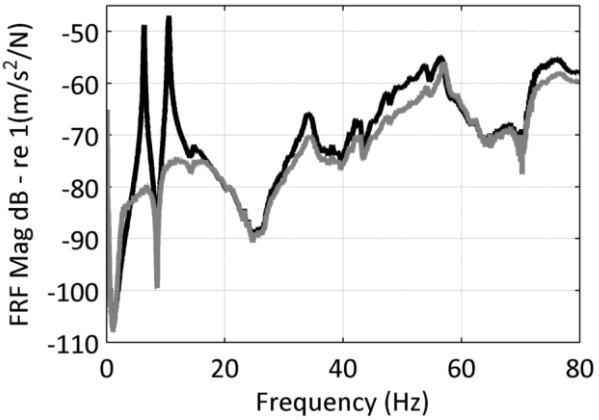

Figures 17. Uncontrolled and controlled FRF trace for compensator referenced as 10 in Table 8

6. Conclusions

This paper has been focused on active vibration suppression of human-induced vibrations in a walkway bridge structure in the Forum Building, University of Exeter. It has compared the vibration mitigation performances of two sets of controller schemes implemented in a SISO set-up: (1) a proportional-integral (PI) controller based on measured walkway bridge acceleration response, and (2) a series of reduced-order observer controllers formulated from a single and three structural vibration modes, respectively, also based on measured walkway bridge acceleration response.

PI controllers are attractive in the sense that they are quicker to formulate and they do offer appropriate enhancement to the damping properties of the walkway bridge structure. Even without suitable plant models, the gains can easily be fine-tuned for this application. For purely SISO schemes, they attenuate resonant frequencies observable at a particular controller location.

With the observer-based (dynamic) compensators, the controller design requires both the selection of desired closed-loop eigenvalues of selected modes of vibration of the walkway bridge structure as well as appropriate observer eigenvalues. This can be quite a rigorous procedure and there is also need for appropriate plant models for their design. It is seen that various reduced order compensator orders can be designed depending on the number of plant modes included in the design and these can be tailored to meet specific objectives. For example, the design of a dynamic compensator based on a single plant mode results in a lossy-integrator type controller that attenuates most frequencies observable at a particular location. Much higher order dynamic compensators, for example, those designed from three plant modes in this work can be tailored for more targeted control, in that control energy can be focused on specific resonances. The compensators are seen to be attractive in the sense that they possess low gains at low frequencies and also possess appropriate roll-off behaviour at higher frequencies. As numerous solutions are possible with this design approach, optimisation algorithms can be introduced or formulated to search for solutions within a given search space and some additional specifications, for example, simulation studies can then be undertaken to narrow down to what might be regarded as the ‘best’ solution as seen in this work.

Acknowledgements

The authors would like to acknowledge the financial assistance provided by the UK Engineering and Physical Sciences Research Council (EPSRC) through a responsive grant (Ref. EP/H009825/1), a Platform Grant (Ref. EP/G061130/2) and a Leadership Fellowship Grant (Ref. EP/J004081/2).

7. References

Bandivadekar TP and Jangid RS (2013) Optimization of multiple tuned mass dampers for vibration control of system under external excitation. *Journal of Vibration and Control*, 19 (12): 1854-1871.

BS5400 (1978) Part 2, Appendix C: *Vibration serviceability requirements for foot and cycle track bridges*, Great Britain, 1978.

BS6472-1 (2008) *Guide to evaluation of human exposure to vibration in buildings*. Vibration sources other than blasting, British Standard.

BS6841 (1987) *Guide to measurement and evaluation of human exposure to whole-body mechanical vibration and repeated shock*. British Standard.

Caetano E, Cunha A, Moutinho C and Magalhaes F (2010) Studies for controlling human-induced vibration of the Pedro e Ines footbridge, Portugal. Part 2: Implementation of tuned mass dampers. *Engineering Structures* 32: 1082-1091.

Carpineto N, Lacarbonara W and Vestroni F (2010) Mitigation of pedestrian-induced vibrations in suspension footbridges via multiple tuned mass dampers, *Journal of Vibration and Control*, 2010 16(5): 749-776.

Casado CM, Diaz IM, Sebastian J, Poncela AV and Lorenzana A (2011) Implementation of passive and active vibration control on an in-service footbridge, *Structural Control and Health Monitoring*.

Chung LL, Wu LY and Jin TG (1998) Acceleration feedback control of seismic structures, *Engineering Structures* 20: 62-74.

Design manual for road and bridges: Loads for Highway Bridges: BD 37/01, Highway Agency, London, February 2002.

Diaz IM and Reynolds P (2010) Acceleration feedback control of human-induced floor vibrations, *Engineering Structures* 32: 163-173.

Hanagan LM (2003) Floor Vibration Serviceability: Tips and Tools for Negotiating a Successful Design, *Modern Steel Construction*, April 2003.

ISO 10137 (2007) Bases for design of structures – serviceability of buildings and walkways against vibrations, International Organization for Standardization.

ISO 2631 (1997) Mechanical vibration and shock evaluation of human exposure to whole body vibration.

Li Q, Fan J, Nie J, Li Q and Chen Y (2010) Crowd-induced random vibration of footbridge and vibration control using multiple tuned mass dampers. *Journal of Sound and Vibration* 329: 4068-4092.

Liu GP and Daley S (1998) Stable dynamical controller design for robust polynomial pole assignment. *IEE Proceedings, Control Theory Applications* 145 (3): 259-264.

Liu GP, Duan GR and Daley S (2000) Stable observer-based controller design for robust state-feedback pole assignment. *Proceedings of the Institution of Mechanical Engineers* 214 (1): 313-318.

Moutinho C, Cunha A and Caetano E (2007) Implementation of an active mass damper to control vibrations in a 'lively' footbridge. *III Eccomas Thematic Conference on Smart Structures and Materials*, Gdansk, Poland, July 9-11.

Nyawako DS, Reynolds P and Hudson M (2013) Findings with AVC design for mitigation of human induced vibrations in office floors. In *31st International Modal Analysis Conference (IMAC XXVIII)*, Orange County, California, February 2013.

Park KS, Koh HM, and Seo CW (2004) Independent modal space fuzzy control of earthquake-excited structures. *Engineering Structures* 26: 279-289.

Racic V, Pavic A and Brownjohn JMW (2009) Experimental identification and analytical modelling of human walking forces : Literature review, *Journal of Sound and Vibration* 326: 1-49.

Research Fund for Coal and Steel. HiVoSS: Design of footbridges, 2008.

SETRA/AFGC: Passerelles piétonnes – Evaluation du comportement vibratoire sous l'action des piétons (Footbridges – Assessment of dynamic behaviour under the action of pedestrians), Guidelines, Sétra, March 2006.

Smith AL, Hicks SJ and Devine PJ (2009) *Design of floors for vibration: A new approach* (Revised Edition, February 2009). SCI Publication P354.

Wu JC, Yang JN, and Schmitendorf WE (1998) Acceleration feedback control of seismic structures. *Engineering Structures* 20 (3): 222-236.

Xue D, Chen Y and Atherton DP (2007) *Linear feedback control: analysis and design with Matlab*, ISBN-13: 978-0898716382